Original Article

JCBFM

Journal of Cerebral Blood Flow & Metabolism
2023, Vol. 43(11) 1891–1904

DOI: 10.1177/0271678X231183887
journals.sagepub.com/home/jcbfm
Sage

Spatiotemporal features of neurovascular (un)coupling with stimulus-induced activity and hypercapnia challenge in cerebral cortex and olfactory bulb

Shaun James[1], Simon Sanggaard[2], Adil Akif[2], Sandeep K Mishra[1], Basavaraju G Sanganahalli[1], Hal Blumenfeld[3,4], Justus V Verhagen[4,5], Fahmeed Hyder[1,2] and Peter Herman[1]

Abstract

Carbon dioxide (CO_2) is traditionally considered as metabolic waste, yet its regulation is critical for brain function. It is well accepted that hypercapnia initiates vasodilation, but its effect on neuronal activity is less clear. Distinguishing how stimulus- and CO_2-induced vasodilatory responses are (dis)associated with neuronal activity has profound clinical and experimental relevance. We used an optical method in mice to simultaneously image fluorescent calcium (Ca^{2+}) transients from neurons and reflectometric hemodynamic signals during brief sensory stimuli (i.e., hindpaw, odor) and CO_2 exposure (i.e., 5%). Stimuli-induced neuronal and hemodynamic responses swiftly increased within locally activated regions exhibiting robust neurovascular coupling. However, hypercapnia produced slower global vasodilation which was temporally uncoupled to neuronal deactivation. With trends consistent across cerebral cortex and olfactory bulb as well as data from GCaMP6f/jRGECO1a mice (i.e., green/red Ca^{2+} fluorescence), these results unequivocally reveal that stimuli and CO_2 generate comparable vasodilatory responses but contrasting neuronal responses. In summary, observations of stimuli-induced regional neurovascular coupling and CO_2-induced global neurovascular uncoupling call for careful appraisal when using CO_2 in gas mixtures to affect vascular tone and/or neuronal excitability, because CO_2 is both a potent vasomodulator and a neuromodulator.

Keywords

Calibrated fMRI, hypercapnia, near infrared spectroscopy, neurovascular coupling, vascular reactivity

Received 31 January 2023; Revised 12 May 2023; Accepted 15 May 2023

Introduction

The concept of neurovascular coupling refers to chemical signalling in the neuropil that links cellular activity to dynamic hemodynamic alterations,[1] mechanisms[2] which strive to match the high metabolic demands of synaptic activity[3,4] by increasing local cerebral blood flow (CBF) and/or volume (CBV) to deliver more nutrients for oxidative and glucose metabolism (CMR_{O2} and CMR_{glc}).[5,6] Impaired neurovascular coupling indicates onset of pathology as implicated in healthy aging, ischemia, or neurodegeneration.[7,8]

[1]Department of Radiology and Biomedical Imaging, Yale University, New Haven, CT, USA
[2]Department of Biomedical Engineering, Yale University, New Haven, CT, USA
[3]Department of Neurology, Yale University, New Haven, CT, USA
[4]Department of Neuroscience, Yale University, New Haven, CT, USA
[5]John B. Pierce Laboratory, New Haven, CT, USA

Corresponding authors:
Peter Herman, Yale University School of Medicine, 300 Cedar St, TAC, N140, New Haven, CT-06510, USA.
Email: peter.herman@yale.edu

Fahmeed Hyder, Yale University School of Medicine, 300 Cedar St, TAC, N143, New Haven, CT-06510, USA.
Email: fahmeed.hyder@yale.edu

Moreover, neurovascular coupling is also critical for techniques that use hemoglobin (Hb) in blood circulation as the image contrast mechanism like functional MRI (fMRI) and near-infrared spectroscopy (fNIRS).[9,10] Each component of Hb, i.e., oxyhemoglobin (oxyHb) and deoxyhemoglobin (deoxyHb), have different magnetic and optical properties, thereby altering ratios of oxyHb to deoxyHb within perfusing blood vessels can affect the blood oxygenation level dependent (BOLD) contrast in fMRI and fNIRS scans.

Carbon dioxide (CO_2) is often thought of as a simple end gas product to be disposed as waste.[11] However, tight regulation of CO_2 within the neuropil is critical for normal brain function[12] as it impacts respiratory drive, affinity of oxygen binding to Hb, vascular tone to dilate or constrict blood vessels, and interstitial acidity.[13] Although CO_2 is internally generated as a localized end-product of nutrient oxidation (as reflected in CMR_{O2} and CMR_{glc}) following an intense change in neuronal activity, its global concentration can be artificially enriched through inhalation, presumably without affecting CMR_{O2} and/or CMR_{glc}.

Deviations from normal CO_2 levels (i.e., 35–45 mmHg; normocapnia) include scenarios of increased CO_2 (i.e., >45 mmHg; hypercapnia) or decreased CO_2 (i.e., <35 mmHg; hypocapnia). Hypercapnia and hypocapnia are widely used in clinical and experimental realms. Since altering the CO_2 in gas mixtures is repeatedly employed in clinical practice (e.g., for neuroprotective measures[14]) and to improve neuroimaging contrast (e.g., in calibrated fMRI[15]) it is essential to classify the degree to which vascular responses to stimulus-induced activity and hypercapnia are (un)correlated with neuronal activity, both spatially and temporally.

Interstitial CO_2 has direct influence on tissue pH because CO_2 reacts with water to produce carbonic acid (i.e., H_2CO_3) that spontaneously dissociates to form protons (H^+) and bicarbonate (HCO_3^-).[16] Considering interstitial pH affects polarization of cell membranes[17–20] and hypercapnia has been thought to act as an anesthetic[21] by decreasing neuronal excitability,[18] inhaled CO_2 may be a potent neuromodulator. Conversely, hypocapnia increases neuronal excitability and is used clinically not only to induce seizures[22] but also prolong the seizure epochs for therapeutic benefit as in electroconvulsive therapy.[23]

Additionally, acidic pH originating from high CO_2 levels activates voltage-gated potassium (K^+) channels to hyperpolarize endothelial cells. Thus, interstitial CO_2 acts as a powerful vasomodulator.[24] Short-lived epochs of hypercapnia and hypocapnia have opposite effects on cerebral vasculature promoting vasodilation and vasoconstriction, respectively.[25] Since CO_2 is a potent vasodilator, it affects the radius of the vessels causing fourth order change in CBF and a second order change in CBV,[26] but altering CO_2 concentration is commonly viewed as a safe and easy tool by neuroimaging methods like fMRI and fNIRS to alter contrast.[27,28]

We used widefield optical imaging with transgenic mice, expressing genetically encoded calcium (Ca^{2+}) indicators (GECIs),[29] to concurrently map fluorescent Ca^{2+} transients from neurons and reflectometric Hb signal to examine neurovascular coupling. Our results show hypercapnia transiently suppresses brain-wide neuronal activity during CO_2-induced vasodilation. The spatiotemporal patterns of neurovascular uncoupling with hypercapnia are starkly different from the classical neurovascular coupling observed with stimuli-induced responses. Thus, we encourage restraint when using CO_2 in gas mixtures to affect neuronal excitability for neuroprotective measures and/or vascular tone for altering neuroimaging contrast. Our results emphasize that CO_2 is potent in both neuromodulation and vasomodulation, and should not be viewed simply as a metabolic waste product.

Materials and methods

Mice preparation

All mice were housed on a 12-hour light/dark cycle. Food and water were available ad libitum. Male and female mice were adults, 6–12 weeks old, 25–30 g, at time of imaging. Three strains of mice were used: Thy1-GCaMP6f (n = 10), OMP-GCaMP6f (n = 15), Thy1-jRGECO1a (n = 4). The cortical mouse strain Thy1-GCaMP6f was made by the Genetically Encoded Neuronal Indicator and Effector (GENIE) Project. It produces green fluorescent calcium (Ca^{2+}) indicator, GCaMP6f, in Thy1-expressing pyramidal neurons in the cerebral cortex and is commercially available from Jackson Labs (JAX 024339, GP5.11 line). The olfactory mouse strain OMP-GCaMP6f, where OMP stands for olfactory marker protein, was bred using floxed-GCaMP6f reporter mice (JAX 024105) crossed with OMP-Cre mice (JAX 006668).[30] The resulting OMP-GCaMP6f mice have GCaMP6f expression to study olfactory receptor input neurons in the glomerular layer of the olfactory bulb. Another cortical mouse strain Thy1-jRGECO1a was also made by the GENIE Project and produces red fluorescent Ca^{2+} indicator, jRGECO1a, in Thy1 expressing pyramidal neurons in the cerebral cortex and is also commercially available (JAX # 030536, GP8.31 line).

All surgical procedures were approved by the Yale University Institutional Animal Care and Use Committee (IACUC) and follow the National

Institute of Health (NIH) Guide for the Care and Use of Laboratory Animals. All procedures complied with the regulations of the Animals (scientific procedures) Act 1986 and reporting follows the ARRIVE (animal research: reporting of in vivo experiments) guidelines. We created closed cranial windows above the cerebrum and the olfactory bulb of the mouse head at least 5 days before the first experimental recording. This optical window technique was specially developed with four goals in mind: i) to fix the mouse head with a non-metal head holder; ii) to allow mesoscopic optical measurement from the surface of the brain; iii) to allow for MRI compatibility for recordings of mouse brain without susceptibility effect of the cranial window or head fixation; iv) to keep the cranial window clear and secure for months (Supplementary Methods and Figure S1A).

Multi-modal optical imaging setup

The optical setup was designed to measure wide-field Ca^{2+} fluorescent and reflectometric CBV signals using the same filter and camera configuration (Figure 1), and the distance between the cranial window and the tip of the camera setup was fixed. For Thy1-GCaMP6f and OMP-GCaMP6f mice, data were collected alternating the green fluorescent Ca^{2+} image and the reflectometric CBV image (Figure 1(a)). The GCaMP6f fluorophore was excited with a blue light emitting diode (LED) by Thorlabs M470F3 and bandpass filtered (ET460/30x, Chroma Technology Corporation, Bellows Falls, VT) between 443 and 487 nm (Figure 1(b)). Since we measured the reflectometric signal at 570 ± 5 nm (FB570-10, Thorlabs, Newton, NJ) using a Thorlabs M565F3 LED (Figure 1(b)), we avoided the classic beam splitter/dichroic mirror approach and instead illuminated the surface directly with both light sources as close to perpendicular as the optical setup allowed. Before the experiments we made sure that the illuminating light intensities were as even on the brain surface as possible. The reflected and emitted fluorescent signals were targeted to enter to a built in-house objective, which contained two achromatic doublets (AC050-010-A and AC080-010-A, Thorlabs, Newton, NJ) with a 1 mm radius aperture and a 500 nm longpass filter (FELH0500, Thorlabs, Newton, NJ), and connected to a Rolera-XR camera (QImaging Corporation, Surrey, BC) with 2/3-inch CCD array, 12-bit image collection, and 696×520 image resolution. The 500 nm longpass filter allowed both the fluorescent and reflectometric images to be collected by multiplexing. The images were collected with MATLAB Image Acquisition Toolbox (R2019) (The Mathworks Inc., Natick, MA) and the LEDs were switched in synchrony with the camera triggers by CED μ1401 and Spike2 (Cambridge Electronic Design Ltd, Cambridge, UK).

The 570 nm reflectometric signal was recorded at an isosbestic point of Hb (Figure 1(b)), i.e., the oxygen saturation of Hb does not influence the CBV signal intensity. We assumed that we measured the changes of the total Hb concentration (i.e., [oxyHb] + [deoxyHb]) which is the negative equivalent of the CBV change. This reflected signal was also used for

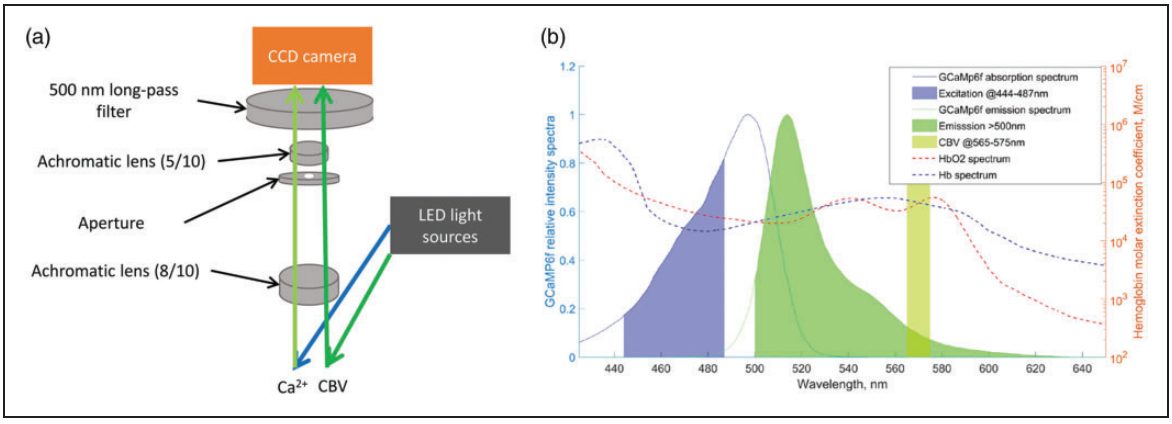

Figure 1. Dual channel optical recordings of wide-field Ca^{2+} fluorescent and reflectometric CBV signals. (a) The in-house optical assembly includes two achromatic lenses (5- and 8-mm diameter each with 10 mm focal distances), a 1 mm hole (aperture) and a 500 nm long-pass filter. The blue light absorbed by GCaMP6f, producing green Ca^{2+} fluorescence, was recorded with a CCD camera. The alternating green light source at 570 nm (above the absorption spectrum of GCaMP6f) reflects from the tissue and recorded by multiplexing and (b) The theoretical GCaMP6f excitation and emission spectra are shown on the left axis, normalized to their peak value. We recorded above 500 nm in the shaded green area for Ca^{2+} fluorescent signal and in the 570 ± 5 nm range (green-yellow area) for the reflected ΔCBV signal. On the right axis we show the molar extinction coefficient for oxyhemoglobin (HbO_2) and deoxyhemoglobin (Hb). Note that in the shaded areas the absorption of the two chromophores are almost equal (45195 M/cm for Hb and 44729 M/cm for HbO_2), only 1% difference.

hemodynamic correction of the fluorescent Ca^{2+} signal. The fluorescent Ca^{2+} signal change was equivalent to the variation of Ca^{2+} ion intracellular concentration in the observed area. In Thy1-GCaMP6f and Thy1-jRGECO1a mice the Ca^{2+} signal reflected the change of the excitatory neuronal activity, whereas for OMP-GCaMP6f mice the Ca^{2+} signal described the olfactory input to glomeruli. For Thy1-jRGECO1a mice, we used a similar optical setup, but the Ca^{2+} excitation wavelength was 560 ± 40 nm and recorded above a 600 nm cutoff, whereas the CBV was determined by measuring Hb absorption at 685 nm and 800 nm isosbestic wavelengths.

Experimental setup for multi-modal imaging and physiological monitoring

On the day of the experiment the surgically prepared and spontaneously breathing mice were anesthetized with 0.25–0.5% isoflurane and subcutaneous infusion of dexmedetomidine, an α2-adrenergic receptor agonist (Dexdomitor, Covetrus, Elizabethtown, PA), with 0.25 mg/kg/hour dosage. The mice were laid in supine position on a heated platform (ATC1000, World Precision Instruments, Saratoga, FL) with the head-post fixed to a stand. LED lights illuminated the optical window evenly through fiber optics as close to perpendicular to the cranial window as possible. The camera was positioned exactly above the head with a micromanipulator. Rectal temperature and respiration were continuously recorded during the experiment. The respiration rate was measured with a laser Doppler probe (Oxyflow 2000; Oxford Optronics, Oxford, UK) positioned to the chest wall allowing spontaneous breathing movement recorded in the laser Doppler signal.

We obtained cortical data from Thy1-GCaMP6f and Thy1-jRGECO1a mice, and bulbar data from OMP-GCaMP6f mice. In Thy1-GCaMP6f and Thy1-jRGECO1a mice two stimulating electrodes were attached to the hindpaw, between toes 1–2 and 4–5 with removable microclips. The conductivity between skin and electrodes was increased with electrode gel. Hindpaw stimulation was provided by a stimulus/isolator unit (A365, WPI, Inc, Saratoga, FL), which was controlled by the Spike2 software. Stimulation parameters were 1–1.5 mA, 10 Hz, with 1% duty cycle for 30 s duration. The 10 Hz stimulation was selected for maximal response under the selected anesthesia,[31–33] and either 1 or 1.5 mA were used to evoke a response (without muscular contractions) that differentiated from baseline noise. In OMP-GCaMP6f mice the odor stimulation was 10% of ethyl-butyrate in mineral oil perfused with the breathing air using Spike2 controlled solenoids for 30 s.[34,35] Hypercapnic challenges were performed by adding 5% CO_2 (inducing ~50 mmHg $PaCO_2$[36]) to the breathing gas mixture for 30 s by the Spike2 controlled solenoids.[37,38] During the hypercapnic episode the percentage of other gases decreased, but we avoided hypoxia because the breathing gas mixture (N_2: 72%, O_2: 28%) has slightly higher O_2 concentration, which provided normoxic O_2 concentration even during the hypercapnic challenge. The mice and the whole experimental setup during recording were positioned in a black box to avoid ambient light contamination from the room. We first measured stimulation-induced CBV and Ca^{2+} responses in the cerebral cortex or the olfactory bulb, and then we applied hypercapnic challenges. Thereafter, stimulation and hypercapnic challenges were repeated several times in random order.

Data processing for Ca^{2+} fluorescent and CBV reflectometric signals

Multi-modal data were collected with 10 fps temporal resolution using 60 ms exposure time (i.e., 60% duty cycle). Ca^{2+} and CBV data were collected alternatively (multiplexed recording), where the switch on/off cycles of the two different light sources were not overlapped to minimize cross-contamination. Data were cropped to the embedding rectangular area of cortex/bulbar to decrease file size. Then images were separated into raw Ca^{2+} and CBV signals. Since imperfections created during optical window preparation can locally alter the recorded signal, such areas were identified in the vessel/anatomical image and excluded from further analysis for both Ca^{2+} and CBV signals. Both Ca^{2+} and CBV data were adjusted by the dark image (collected only with ambient light). Since the origins of the two signals were different, further analysis required different preprocessing steps. For example, for GCaMP6f the green emitted Ca^{2+} fluorescence signal is obtained with blue excitation to calculate fluorescence change ($\Delta F/F_0$). While the emitted light intensity depends on the Ca^{2+} ion flux (measured $\Delta F/F_0$ signal), the surrounding Hb can absorb the emitted green light (attenuated $\Delta F/F_0$ signal). Since both Ca^{2+} and CBV signals change were measured concurrently, we needed local information of Hb in the vicinity of the emitted green light (i.e., same pixel) to correct the Ca^{2+} intensities. We achieved this by measuring the attenuation of the reflectometric 570 nm light. The 570 nm is one of the isosbestic points of the oxyHb and deoxyHb absorption curves, so the oxygenation change of the Hb did not confound this reflectometric signal to represent CBV changes in the region of interest (ROI). Based on the modified Beer-Lambert equation, we used the

raw CBV and raw Ca^{2+} signals to estimate the corrected Ca^{2+} signal (Figure S1B),[39–41]

$$\text{corrected Ca}^{2+} = \text{raw Ca}^{2+} \times \exp[-\ln(\text{raw CBV}) \times d(\text{GFP}) \times \varepsilon(\text{GFP})/d(\text{CBV})/\varepsilon(\text{CBV})]$$

where d(GFP) and d(CBV) are the mean optical pathlength of emission of green fluorescent protein (GFP) at 500–530 nm and the mean optical pathlength of CBV signal at 570 nm, 270 and 280 μm, respectively,[39–41] and ε(GFP) and ε(CBV) are the molar extinction coefficients of averaged Hb at the same wavelengths, 20897.4 cm^{-1} M^{-1} and 44784 cm^{-1} M^{-1}, respectively, as previously described by Scott Prahl (https://omlc.org/spectra/hemoglobin). Thus, all presented data will show the hemodynamically corrected Ca^{2+} signal. We also simulated the corrected Ca^{2+} signals by modifying the second part of the equation from 20% to 240% of the original value to estimate the potential error of hemodynamic under-correction of the hypercapnic Ca^{2+} signal (Figure S1C). We found that not even 180% change can completely nullify the Ca^{2+} signal change.

Because of fast, burst-like Ca^{2+} fluorescence activity in the cortex, we generated Student's t-test maps by comparing the resting period to consecutive 1 s bins for the entire 30 s stimulation epoch (using ttest2 function in Matlab), where the aggregate was Gaussian filtered with a kernel size of 3 to generate (de)activated t-map ROIs. We extracted the average time series from those ROI voxels where the p-value was smaller than 0.05. The same process was applied for the CBV data. Trial based time-courses were averaged pixel-wise and shown as their mean and standard deviation (SD), unless otherwise specified. Overlap of the Ca^{2+} and CBV t-maps were calculated as the Sørensen-Dice similarity coefficient (using dice function in MATLAB). We also calculated time-to-peak (TTP) and return-to-rest time (RRT).

Results

We measured the raw fluorescent Ca^{2+} signal from the cerebral cortex (hindpaw (HP) stimulus and CO_2 exposure) and olfactory bulb (odor stimulus and CO_2 exposure) along with the reflectometric Hb absorption change at the isosbestic wavelength. The reflectometric signal was used to calculate the CBV change from the same spatial location as the Ca^{2+} signal and for hemodynamic correction of the fluorescent Ca^{2+} signal.[39–41] The sensory stimulation data were needed to confirm that the hypercapnia data are physiologically relevant. Moreover, data from the bulb and cortex were used to confirm universality of responses to sensory and CO_2 stimuli. Respiratory rate significantly changed from 138 ± 11 breaths/min at baseline to 213 ± 33 breaths/min during CO_2 exposure and returned to 134 ± 10 breaths/min one minute after cessation of hypercapnic challenge.

Cortical recordings

During HP stimulation bilaterally localized cortical activations were observed in both Ca^{2+} and CBV t-maps, as shown from one representative Thy1-GCaMP6f mouse (Figure 2(a)) and across other Thy1-GCaMP6f mice (Figure S2A), where the spatial overlap between Ca^{2+} and CBV t-maps was ~75% (Table S1).

Cortical Ca^{2+} and CBV responses with HP stimulation exhibited rapid signal increase/decrease coinciding well with stimulus onset/offset timing, indicating strong neurovascular coupling (Figure 2(b) and (e)). In Thy1-GCaMP6f mice the TTP with HP stimulation for cortical Ca^{2+} response (~7 s) was faster than the cortical CBV response (~14 s), whereas the RRT were quite similar (~22 s) for cortical Ca^{2+} and CBV responses (Table S2). Average magnitudes of cortical Ca^{2+} and CBV responses were +0.3% and +1.3%, respectively.

Upon CO_2 exposure bilateral global increases were detected in cortical CBV t-map but with bilateral global deactivation in cortical Ca^{2+} t-map, as shown in the same representative Thy1-GCaMP6f mouse (Figure 2(c)) and across other Thy1-GCaMP6f mice (Figure S2B). Despite neurovascular uncoupling with CO_2 exposure, the spatial overlap between cortical Ca^{2+} and cortical CBV t-maps was ~96% (Table S1).

CO_2-induced cortical Ca^{2+} and CBV responses exhibited very slow, but global, signal increase/decrease coinciding poorly with onset/offset timing of CO_2 exposure (Figure 2(d)), indicating distinct spatiotemporal patterns of neurovascular uncoupling (Figure 2(f)). In Thy1-GCaMP6f mice, the TTP for CO_2-induced cortical Ca^{2+} response (~30 s) was similar to CO_2-induced cortical CBV response (~36 s), whereas the RRT were quite similar (~50 s) for the CO_2-induced Ca^{2+} and CBV responses (Table S2). Average magnitudes of cortical Ca^{2+} and CBV responses were, respectively, −0.5% and +3.0% for the entire CO_2 exposure epoch, respectively.

We also recorded from Thy1-jRGECO1a mice which emit red Ca^{2+} fluorescence (Figures 3 and S3). In Thy1-jRGECO1a mice HP-induced and CO_2-induced changes were comparable to observations in Thy1-GCaMP6f mice. In Thy1-jRGECO1a mice the spatial overlap between cortical Ca^{2+} and CBV t-maps was also high, with HP stimulation (Figure 3(a)) and

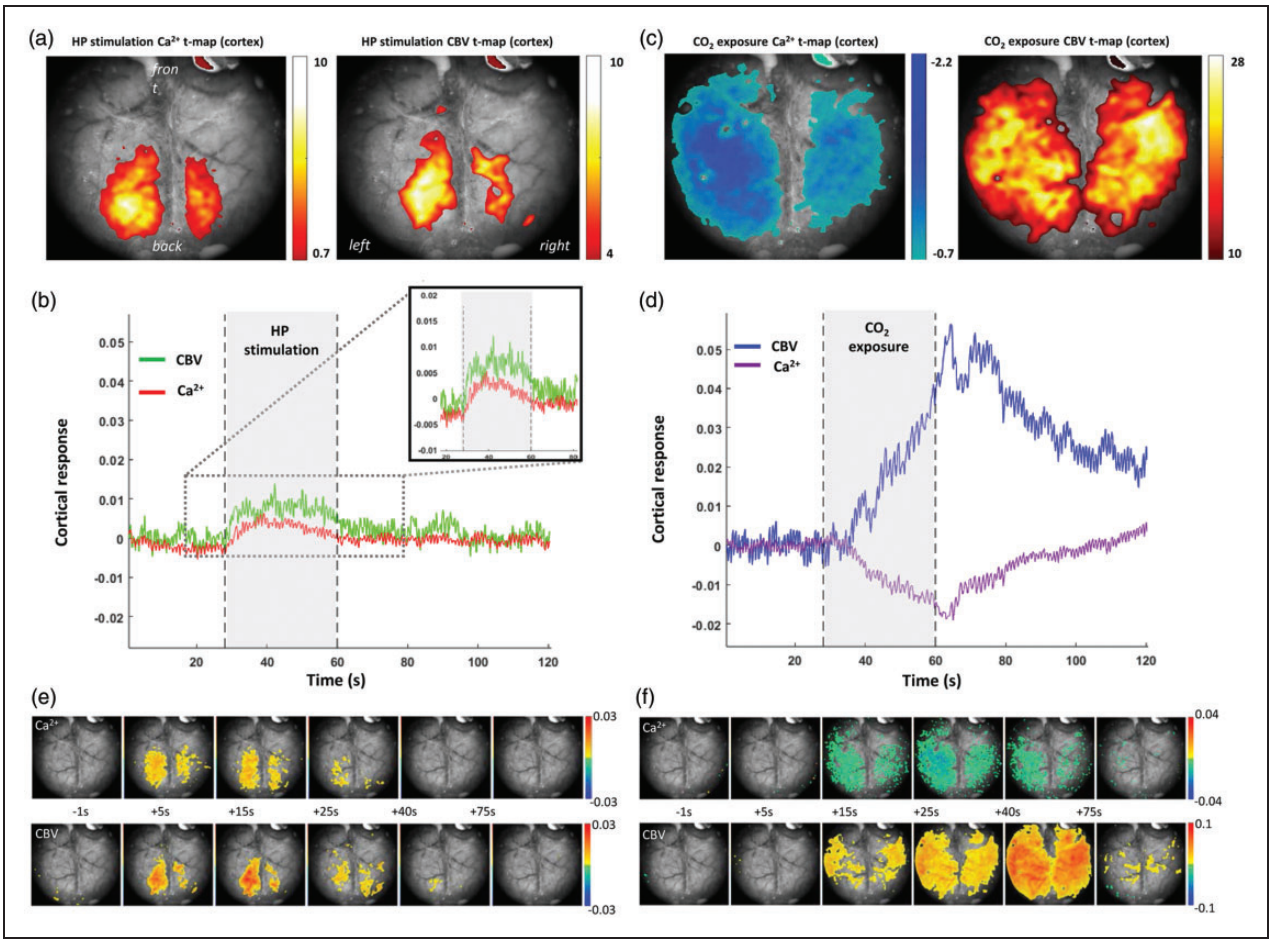

Figure 2. Representative single trial data from one Thy1-GCaMP6f mouse during hindpaw (HP) stimulation and hypercapnia challenge (or CO_2 exposure). During HP stimulation cortical (a) t-maps of Ca^{2+} (left) and CBV (right) signals, and (b) temporal responses of Ca^{2+} (red) and CBV (green) signals. With HP stimulation there is marked increase in Ca^{2+} signal during increase in CBV signal. During CO_2 exposure cortical (c) t-maps of Ca^{2+} (left) and CBV (right) signals, and (d) temporal responses of Ca^{2+} (purple) and CBV (blue) signals. With CO_2 exposure there is marked decrease in Ca^{2+} signal during increase in CBV signal. (e–f) Spatiotemporal neurovascular coupling and uncoupling in cerebral cortex during stimulation and hypercapnia from the same Thy1-GCaMP6f mouse. Ca^{2+} (top) and CBV (bottom) activity patterns are shown relative to the start of the of hypercapnic challenge (30 s in absolute time) with 1 s binned maps.

CO_2 exposure (Figure 3(b)). In Thy1-jRGECO1a mice the TTP for CO_2-induced cortical Ca^{2+} response (~32 s) was similar to the CO_2-induced cortical CBV response (~33 s), whereas the RRT were quite similar (~50 s) for the CO_2-induced Ca^{2+} and CBV responses (Figure 3(c)).

Bulbar recordings

During odor stimulation bilaterally localized bulbar activations were observed in both Ca^{2+} and CBV t-maps, as shown from one representative OMP-GCaMP6f mouse (Figure 4(a)) and across other OMP-GCaMP6f mice (Figure S4A), where the spatial overlap between the bulbar Ca^{2+} and CBV t-maps was ~87% (Table S1).

Odor-induced bulbar Ca^{2+} and CBV responses exhibited rapid signal increase/decrease coinciding well with stimuli onset/offset timing (Figure 4(b)), indicating well-accepted neurovascular coupling. In OMP-GCaMP6f mice, the TTP for odor-induced bulbar Ca^{2+} response (~1 s) was much faster than the odor-induced bulbar CBV response (~5 s), whereas the RRT were quite similar (~27 s) for the odor-induced bulbar Ca^{2+} and CBV responses (Table S2). Magnitudes of bulbar Ca^{2+} and CBV responses were, respectively, +3.3% and +1.1% for the entire odor stimulation duration.

During CO_2 exposure bilateral global increase was measured in the bulbar CBV t-map and bilateral global deactivation was observed in the bulbar Ca^{2+} t-map, as shown in the same representative OMP-GCaMP6f mouse (Figure 4(c)) and across other OMP-GCaMP6f mice (Figure S4B), where the spatial overlap between bulbar Ca^{2+} and CBV t-maps was ~82% (Table S1).

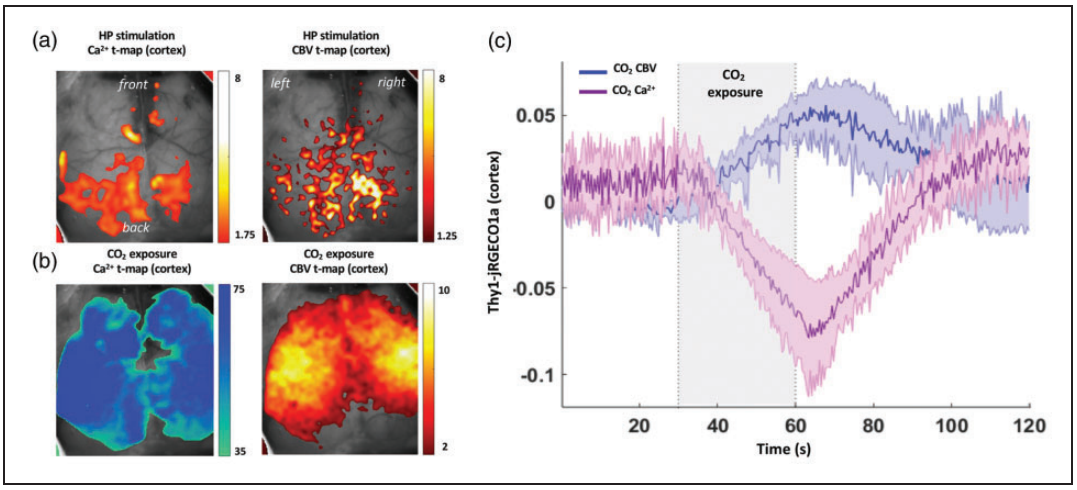

Figure 3. Representative data from one Thy1-jRGECO1a mouse during hindpaw (HP) stimulation and hypercapnia challenge (or CO_2 exposure). (a) During HP stimulation cortical t-maps of Ca^{2+} (left) and CBV (right) signals. (b) During CO_2 exposure cortical t-maps of Ca^{2+} (left) and CBV (right) signals. Both (a) and (b) show single trial data. (c) Averaged (mean ± SD) dynamics for all responses of cortical Ca^{2+} (purple) and CBV (blue) signals during CO_2 exposure all Thy1-jRGECO1a mice (n = 4) shown in fractional changes.

CO_2-induced bulbar Ca^{2+} and CBV responses exhibited very slow, but global, signal increases/decreases delayed from the onset/offset timing of CO_2 exposure (Figure 4(d)), indicating noticeable spatiotemporal features of neurovascular uncoupling (Figure 4(f)). In OMP-GCaMP6f mice the TTP for CO_2-induced bulbar Ca^{2+} response (~27 s) was similar to the CO_2-induced bulbar CBV response (~32 s), whereas the RRT were quite similar (~32 s) for the CO_2-induced Ca^{2+} and CBV responses (Table S2). Magnitudes of bulbar Ca^{2+} and CBV responses were, respectively, −1.0% and +1.0% for the entire CO_2 exposure epoch.

Comparison of dynamic Ca^{2+} and CBV responses with HP/odor stimuli and CO_2 exposure

Overall dynamic patterns of Ca^{2+} and CBV responses obtained from all Thy1-GCaMP6f (n = 10) and OMP-GCaMP6f (n = 15) mice (Figure 5; Tables S1, S2) showed similar trends as the individual GCaMP6f mice (Figures 2, S2, 4, S4). While Ca^{2+} responses to hypercapnia in the cortex and bulb were quite similar in amplitude and dynamics, the magnitude of the Ca^{2+} response to HP stimulation was significantly lower than with odor stimulation (Figures 5(a) and (b)). However, the Ca^{2+} response to hypercapnia in the bulb had a peculiar signal reversal immediately following the CO_2 offset, a pattern that was not observed in the cortex (Figures 5(a) and (b)). While the CBV responses in the cortex and bulb were generally similar in dynamics, the CBV response to hypercapnia in the cortex was almost four times greater than in the bulb, and moreover, the CBV response in the bulb peaked much earlier than in the cortex (Figures 5(c) and (d)).

Discussion

Regulating CO_2 in the brain is critical[12] due to its impact on factors such as: respiration, oxygen-hemoglobin binding, vascular tone, and interstitial acidity.[13] Although stimulus-induced activity and hypercapnia trigger vasodilation, the mechanisms by which interstitial CO_2 levels are raised differ (by metabolism and inhalation, respectively). Thus, establishing how these vasodilatory responses are (dis)associated with neuronal activity has clinical[17–23] and experimental[24–28] relevance.

We simultaneously measured reflectometric CBV signal and fluorescent Ca^{2+} signal (hemodynamic corrected) from mouse brain (Figures 1 and S1). For cortical recordings we used green fluorescent Ca^{2+} in Thy1-GCaMP6f mice (Figures 2 and S2) and red fluorescent Ca^{2+} in Thy1-jRGECO1a mice (Figures 3 and S3), whereas for bulbar recordings we used green fluorescent Ca^{2+} in OMP-GCaMP6f mice (Figures 4 and S4). These multi-modal recordings were used to examine the neurovascular (un)coupling during stimuli and CO_2 exposure (Figure 5; Tables S1, S2). Our results reveal contrasting effects of hypercapnia on neuronal response (deactivation or decrease) and vasodilatory effects (activation or increase), which are spatiotemporally disassociated in a complex manner when compared to conventional neurovascular coupling, with vasodilation and increased neuronal activity.

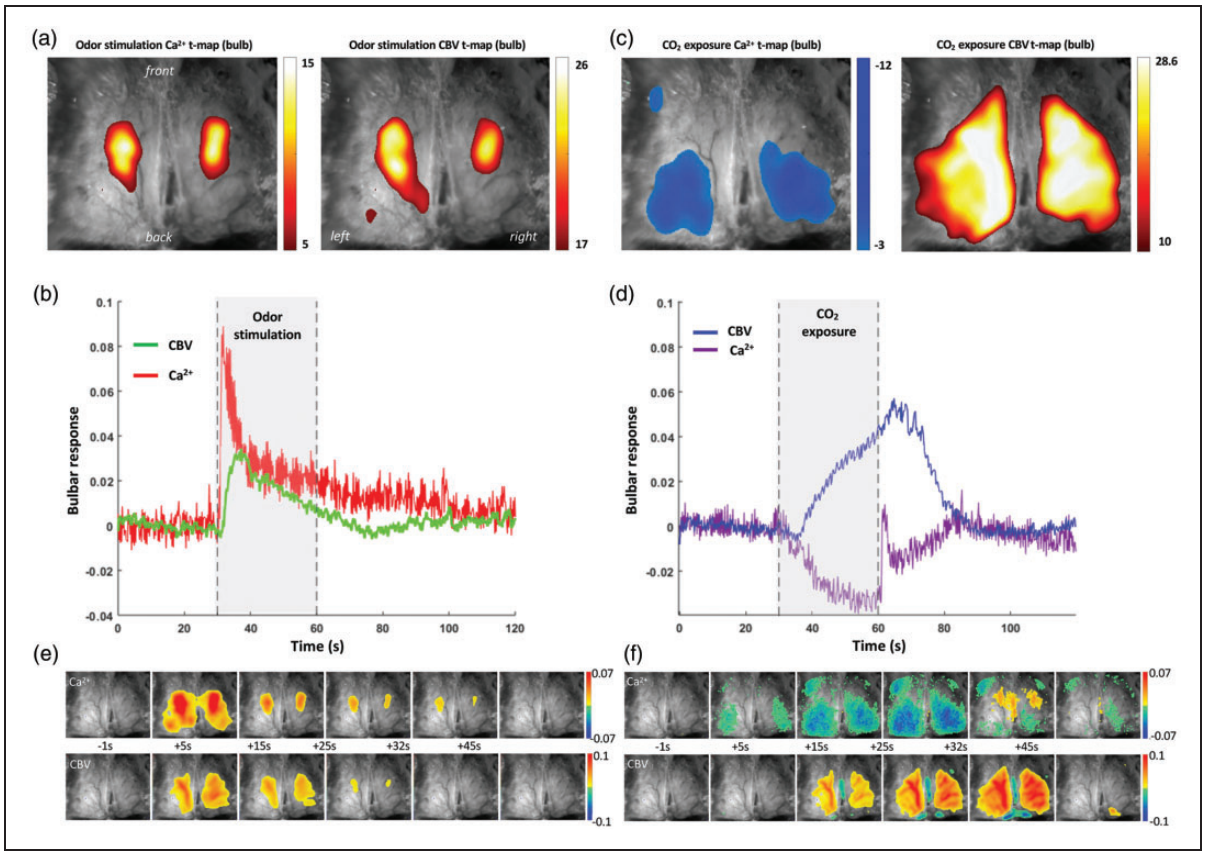

Figure 4. Representative single trial data from one OMP-GCaMP6f mouse during odor stimulation and hypercapnia challenge (or CO_2 exposure). During odor stimulation bulbar (a) t-maps of Ca^{2+} (left) and CBV (right) signals, and (b) temporal responses of Ca^{2+} (red) and CBV (green) signals. With odor stimulation there is marked increase in Ca^{2+} signal during increase in CBV signal. In contrast to the cortical response during hindpaw stimulation, in the bulb there is a sharp increase in Ca^{2+} signal immediately after onset of odor stimulus. During CO_2 exposure bulbar (c) t-maps of Ca^{2+} (left) and CBV (right) signals, and (d) temporal responses of Ca^{2+} (purple) and CBV (blue) signals. With CO_2 exposure there is marked decrease in Ca^{2+} signal during increase in CBV signal. In contrast to the cortical response during CO_2 exposure, in the bulb there is a sharp increase in Ca^{2+} signal immediately after offset of hypercapnia challenge. (e-f) Spatiotemporal neurovascular coupling and uncoupling in olfactory bulb during stimulation and hypercapnia from the same Thy1-GCaMP6f mouse. Ca^{2+} (top) and CBV (bottom) activity patterns are shown relative to the start of the of hypercapnic challenge (30 s in absolute time) with 1 s binned maps.

Technology development to measure brain-wide neurovascular (un)coupling

In conjunction with green and red fluorescent Ca^{2+} signal, the reflectometric CBV signal was measured at two isosbestic points of Hb absorption: at 570 nm to record the green Ca^{2+} signal (in Thy1-GCaMP6f and OMP-GCaMP6f mice) simultaneously with CBV, and at 800 nm to measure the red Ca^{2+} signal (Thy1-jRGECO1a mice) simultaneously with CBV.

Using the GCaMP6f as an example (Figure 1), we recorded the CBV and Ca^{2+} signals in two different spectral bands, one for the green fluorescent signal of neuronal activity and another for the hemodynamic signal of Hb concentration changes. Ideally, the blue absorption spectral band below 490 nm excited the green fluorescent chromophore emitting light within the 500–530 nm band. Applying an appropriate dichroic beamsplitter, the two spectral regimes were well separated to avoid cross-talk. The clear advantage of this widely used method is that the excitation and emitted light go through the same optical system ensuring that only the same areas are illuminated and recorded.[42] The intensity of emitted fluorescent light depends on both the concentration of the fluorophores and the concentration of absorptive chromophores in the tissue. Since we calculate the $\Delta F/F_0$ signal, its value remains stable until there is no time dependent change in the absorptive chromophore concentration. The highest concentration chromophores are the Hb molecules in the cerebral vessels and because of neurovascular coupling the stimulation itself changes not only the neuronal activity but also CBV. Therefore, we had to measure the CBV independently, not only for the hemodynamic response but for the correction of fluorescence signal intensity with the changing Hb

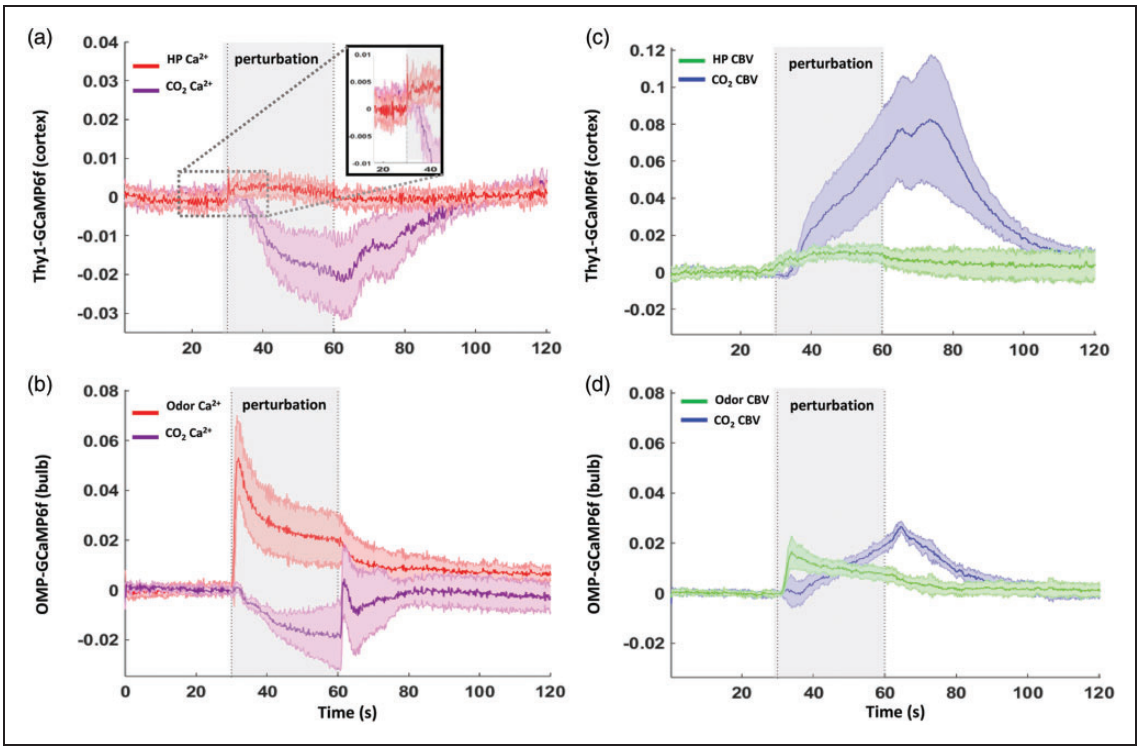

Figure 5. Average (mean ± SD) responses from all Thy1-GCaMP6f (cortical; n = 10) and OMP-GCaMP6f (bulbar; n = 15) mice. (a) Dynamic cortical Ca^{2+} responses during hindpaw (HP) stimulation (red) and CO_2 exposure (purple) from Thy1-GCaMP6f mice. (b) Dynamic bulbar Ca^{2+} responses during odor stimulation (red) and CO_2 exposure (purple) from OMP-GCaMP6f mice. (c) Dynamic cortical CBV responses during hindpaw (HP) stimulation (green) and CO_2 exposure (blue) from Thy1-GCaMP6f mice and (d) Dynamic bulbar CBV responses during odor (green) and CO_2 exposure (blue) from OMP-GCaMP6f mice.

concentration.[39–41] This can be achieved either below the absorption spectrum of the fluorophore with ultraviolet[43,44] or above it with visible light. Since ultraviolet light requires specific lenses and sensitive camera sensor, we used the isosbestic wavelength of Hb absorption at 570 nm. The parallel application of the reflectometric measurement forced us to give up the classic GFP dichroic mirror and emission filter to illuminate the surface separately from the objective. This approach is still viable because Hb absorbance declines rapidly above 550 nm, the higher end emissions can minimally influence the fluorescent signal and the 570 nm is above the absorption spectrum of the green fluorescent Ca^{2+} indicator.

Mechanisms of CO_2-induced neuronal depression and vasodilation

Traditionally CO_2 is simply thought of as a metabolic waste product.[11] However, recent work proposes CO_2 as a mediator of neurovascular coupling,[45] and our results strongly suggest CO_2 is a vasomodulator and a neuromodulator. It is well documented that CO_2 is a potent vasodilator,[24] through a process which involves activating voltage-gated K^+ channels to hyperpolarize endothelial cells. However, the mechanisms of CO_2-induced neuromodulation are more complex, as the CO_2-mediated neuronal inhibition may be due to a combination of direct and indirect mechanisms initiated after hypercapnic onset.

During CO_2 exposure carbonic anhydrase, a ubiquitously expressed enzyme in all cell types, increases extracellular H^+ through the spontaneous $CO_2 + H_2O \rightarrow H^+ + HCO_3^-$ reaction. The subsequent pH reduction is known to blunt neural excitability and disrupt membrane potential regulation by inhibiting voltage-dependent Ca^{2+} channels and hyperpolarization-gated and cyclic nucleotide-activated cation (HCN) channels.[46,47] Additionally, increased arterial CO_2 can give rise to elevated levels of adenosine, a potent neuromodulator, acting through G-protein coupled adenosine A1 receptors to inhibit neuronal activity by inhibiting excitatory Ca^{2+} channels, stimulating inhibitory K^+ channels, or diminishing the excitatory synaptic release of glutamate.[46,48] The rise in interstitial adenosine presumably originates/derives from CO_2-mediated inhibition of adenosine kinase, the enzyme responsible for metabolizing adenosine for the production of ATP, or CO_2/pH

modulation of purinergic receptors on local astrocytes or microglia.[49]

While our results show consistent responses to CO_2 exposure across the surface of the murine brain, we have also identified a novel post-stimulus effect in the olfactory bulb. Immediately following the end of the CO_2 exposure and diminished Ca^{2+} fluctuations, we report a post-stimulus "positive" peak in Ca^{2+} activity (Figure 5(b)). This complex response may be a resulting from activation of acid-sensing ion channels (ASICs) known to be densely expressed in the olfactory bulb[50] and other deeper regions of the brain.[51] Following this mechanism of excitation, the excess H^+ from CO_2 conversion would bind and activate ASICs facilitating cellular influx of sodium (Na^+), increasing neuronal excitability.[52] This may be a protective mechanism against hypercapnic acidosis clearing excess CO_2/H^+, which seems preferential to the bulb.

Features of spatiotemporal neurovascular (un) coupling during induced activity and hypercapnia

The vast difference in the spatial extent of stimuli-induced local neurovascular coupling vs. CO_2-induced global neurovascular uncoupling (Figures 2 and 4) can be explained by specific wiring connections of each stimulus to localized brain regions vs. non-specific distribution of inhaled gas to the entire body. Stimuli-induced CBV increases were temporally shorter than the CO_2-induced in both the cortex and the bulb (Figures 5(c) and (d)). Additionally, the CO_2-induced global neurovascular uncoupling in the cortex produced a much larger peak CBV amplitude compared to the stimuli-induced, while the responses to both challenges were generally similar in amplitude for bulb (Figures 5(c) and (d)). The observed difference in cortical CBV amplitude could be due to a domination of CBV (and BOLD) response from the larger pial vessels which are located mostly in the superficial lamina of the cortex.[53,54] Interestingly, while HP stimulation and CO_2 exposure elicit an increase in CBV, the comparison of Ca^{2+} responses between the two challenges highlights the CO_2-induced neurovascular uncoupling (Figures 5(a) and (b)). The differences in fluorophore distribution in the cortex (diffuse) and the bulb (condensed) further highlight the breadth and magnitude of the neurovascular uncoupling, respectively.

In Thy1-GCaMP6f the source of the cortical Ca^{2+} signal is likely dendrites within the neuropil. A previous calibrated fMRI and electrophysiology study in rat cerebral cortex showed laminar distribution of sensory-evoked electrical activity, where the highest magnitude was located in the middle and deeper layers.[54] In the mouse cerebral cortex[55] we estimate the distance from the surface of the cranial window to the location of highest neuropil density in middle to deeper cortical layers to be 2–3 mm, which is outside the range of fluorescent optical recordings, even with the 1.2–2.5 mm thick transparent region of the cranial window. Similarly, in OMP-GCaMP6f the origin of the bulbar Ca^{2+} signal is olfactory receptor input neuron synapsed in the glomerular layer. A recent fMRI and optical imaging study in the rat olfactory bulb demonstrated highest odor-induced responses in the glomerular layer.[42] In the mouse olfactory bulb[55] we expect the gap from the top of the cranial window to the glomerular layer to be around 1.5 mm. These suggest a factor two higher optical signal for the bulbar data.

As discussed above, the neuronal inhibition effects of CO_2 are multifaceted involving activities of carbonic anhydrase, voltage-dependent Ca^{2+} channels, hyperpolarization-gated and cyclic HCN channels, and adenosine A1 receptors. It is likely these cellular machineries are widely distributed in cerebral cortex and olfactory bulb. However, the presence of a post-stimulus "positive" peak in the bulb (Figure 5(b)) is most likely due to the activity of ASICs, which are more prominent in specific brain regions including the bulb.[50,51]

Impact of current results on using CO_2 gas mixtures in experimental practice

Calibrated fMRI requires measurements of BOLD signal along with CBF and/or CBV to estimate CMR_{O2}.[56] Calibration is often performed using brief exposures to slightly elevated CO_2 with inhaled air to obtain maximal CBF (or CBV) response.[57] This standard method for calibrated fMRI is presumed to purely produce vascular changes in BOLD signal via CBF/CBV, with minimal or no CMR_{O2} changes.[58] However, this iso-metabolic presumption remains under debate due to variations in the duration of the hypercapnic challenge, the concentration of CO_2 inhaled or degree of hypercapnia induced, methods of exposure, techniques used to identify increases in arterial CO_2, and brain regions assessed – all of which contribute to substantial outcome variability in the literature.[15] Some studies demonstrate no statistically significant change in CMR_{O2} with CO_2 concentrations of 5–6%,[59] whereas others have identified either a significant decrease[60–62] or increase[49] in estimated CMR_{O2}. Although these variations in CMR_{O2} estimation may arise due to experimental differences, any CMR_{O2} change with hypercapnia depends on the correlative accuracy of these methods in the absence of actual changes in neuronal activity.

The sensitivity of calibrated fMRI to CMR_{O2} estimation requires an accurate measurement of hemodynamic and neuronal, or lack thereof, responses to hypercapnia. While studies have demonstrated increases, decreases, and no change in CMR_{O2} during hypercapnia,[15] in calibrated fMRI studies hypercapnic challenge is still the most popular method to get the maximal BOLD response while assuming no CMR_{O2} changes. However, gas-free calibrated fMRI methods are available and have been applied in murine and human brain.[63–67] We measured the influence of brief (30 s) and moderate (5% CO_2) hypercapnic exposure on neuronal and hemodynamic activity, and our results clearly show that widespread neuronal activity is indeed influenced by CO_2 with global neurovascular uncoupling.

Avoiding the confounding neurological response to CO_2 can be difficult.[21–24] There are two other methods for calibrated fMRI using gas challenges, hyperoxia and carbogen. A hyperoxic challenge (breathing enriched O_2 typically 50–100% as compared with 21% in normal air) completely avoids the neurological impact of CO_2. However, a pitfall of using hyperoxia is the necessity to assume a constant value of resting oxygen extraction fraction (OEF_0), and hyperoxia has been shown to also impact neural activity.[68] Moreover, carbogen (typically 10% CO_2 balanced with 90% O_2) is favorably viewed as an ideal gas mixture for calibrated fMRI,[69] but based on our findings and those of prior studies[15] we presume that carbogen combines the confounding factors of both hypercapnia and hyperoxia. While gas-free calibrated fMRI using machine learning methods[70] may be the best method to avoid confounding neurological effects, these methods often use a hypercapnic or hyperoxic challenge as a foundation for calibrated fMRI modeling.[71]

Limitations of current study with considerations for future directions

Most human neuroimaging studies which use CO_2 exposure with specific assumptions[15] are conducted in the awake state, whereas most animal studies (like the present one) are executed under different types of anesthetics to achieve different levels of global brain activity.[72] While this may be considered a weakness, we predict that future experiments in the awake mouse paradigm will generate similar results. We selected the anesthetic dexmedetomidine to establish robust neural and hemodynamic responses, since dexmedetomidine anesthesia is generally considered to a level close to the awake state.[33] However, dexmedetomidine alone can cause vasoconstriction and sometimes epileptic responses, therefore we balanced these effects with low dose of isoflurane.[33] Isoflurane alone is not an ideal anesthetic for rodent neuroscience studies because it is known to cause burst-suppression neural activities[73] and cerebral vasodilation.[74] In awake human brain sustained increases in CO_2 suppressed neuronal activity[57,62,75] as measured by magnetoencephalography[62,75] and electroencephalography.[57] However, high CO_2 also depressed neuronal activity in anesthetized non-human primate brain as measured by electrophysiology.[76] These studies, did not measure neuronal and hemodynamic responses to CO_2 concurrently to demonstrate spatiotemporal patterns of uncoupling.

Neuroscience has benefited tremendously from the evolution of GECIs enabling cell-specific recordings of Ca^{2+} activity in brains of transgenic rodents.[29] Two-photon imaging and/or histology can validate location/activity of these cells (excitatory/inhibitory neurons; astrocytes), whereas single-photon mesoscopic Ca^{2+} fluorescence imaging can measure from entire cortical (or bulbar) surfaces. Each imaging modality has its strengths and weaknesses. One weakness in mesoscopic Ca^{2+} fluorescence imaging that we faced was observed in the variations in signal strength in our results. These variations may be attributed to weaker region-specific responses to stimuli or variations in wavelength penetration through surface tissue. Due to these weaknesses, GECI models are constantly being remodeled and refined to produce stronger fluorophore emissions.

A weakness in our present study is that we did not measure astrocytic responses, nor distinguish between glutamatergic and GABAergic neurons. Most GECIs specifically target neurons because there is little (or no) commercially available GCaMP6f or jRGECO1a mouse lines to target astrocytes. For this reason researchers are required to create their own using 'floxed' GECI lines cross-bred with astrocyte-specific expression of Cre-recombinase, or by viral delivery using recombinant AAV vectors.[77]

While this study is similar to prior studies that have combined neuronal signal using either green or red fluorescence with CBV,[39–41] future studies can be designed where the green and red channels are used together to measure from neurons and astrocytes simultaneously. Alternatively, the green or red could be used for either neurons or astrocytes, leaving the other channel to probe cerebral microvessels by using plasma-borne fluorescent probes.[78] This type of multimodal fluorescent imaging would require careful design of optical hardware to measure the CBV signal concurrently.

Conclusion

We utilized novel widefield Ca^{2+} and hemodynamic imaging of the murine cerebral cortex and olfactory bulb to demonstrate complex neurovascular responses

to various stimuli including CO_2. Our current investigation shows that exposure to 5% CO_2 induces vasodilation and neural inhibition simultaneously across large swathes of the brain. These findings challenge the experimental validity of using CO_2 inhalation in calibrated fMRI experiments, specifically when these epochs of gas exposure are not brief. Other clinical applications to modify vascular tone should also consider the neuromodulating capacity of CO_2.

Funding

This work was supported by NIH grants (R01-MH067528, R01 NS100106, R01 DC014723-05S1, T32 DA022975).

Acknowledgements

We thank Jessica Goas Santana for technical support. We thank Joel Greenwood and the Neurotechnology Core in Kavli Institute for Neuroscience for cutting glasses to the cranial windows.

Declaration of conflicting interests

The author(s) declared no potential conflicts of interest with respect to the research, authorship, and/or publication of this article.

Authors' contributions

S.J., F.H., P.H., J.V.V., S.K.M., H.B., and B.G.S. designed research and experiments. S.J., P.H., and S.S. conducted the surgeries. P.H., F.H., S.J., and S.S. designed and constructed the imaging apparatus and collected the data. S.J., P.H., and F.H. analyzed the data. P.H., F.H., A.A., and S.S. contributed code for the analysis of the data. S.J., F.H., and P.H. wrote the manuscript with critical review by all other authors.

ORCID iDs

Adil Akif https://orcid.org/0009-0002-5591-0856
Sandeep K Mishra https://orcid.org/0000-0002-1016-0206
Peter Herman https://orcid.org/0000-0003-2218-9652

Supplementary material

Supplemental material for this article is available online.

References

1. Roy CS and Sherrington CS. On the regulation of the blood-supply of the brain. *J Physiol* 1890; 11: 85–158.17.
2. Zhu WM, Neuhaus A, Beard DJ, et al. Neurovascular coupling mechanisms in health and neurovascular uncoupling in Alzheimer's disease. *Brain* 2022; 145: 2276–2292.
3. Yu Y, Herman P, Rothman DL, et al. Evaluating the gray and white matter energy budgets of human brain function. *J Cereb Blood Flow Metab* 2018; 38: 1339–1353.
4. Yu Y, Akif A, Herman P, et al. A 3D atlas of functional human brain energetic connectome based on neuropil distribution. *Cereb Cortex* 2022; 33: 3996–4012.
5. Hyder F, Patel AB, Gjedde A, et al. Neuronal-glial glucose oxidation and glutamatergic-GABAergic function. *J Cereb Blood Flow Metab* 2006; 26: 865–877.
6. Hyder F, Sanganahalli BG, Herman P, et al. Neurovascular and neurometabolic couplings in dynamic calibrated fMRI: transient oxidative neuroenergetics for block-design and event-related paradigms. *Front Neuroenerg* 2010; 2: 10–3389. /fnene.2010.00018.
7. Girouard H and Iadecola C. Neurovascular coupling in the normal brain and in hypertension, stroke, and Alzheimer disease. *J Appl Physiol (1985)* 2006; 100: 328–335.
8. Stackhouse TL and Mishra A. Neurovascular coupling in development and disease: focus on astrocytes. *Front Cell Dev Biol* 2021; 9: 702832.
9. Huneau C, Benali H and Chabriat H. Investigating human neurovascular coupling using functional neuroimaging: a critical review of dynamic models. *Front Neurosci* 2015; 9: 467.
10. Pinti P, Siddiqui MF, Levy AD, et al. An analysis framework for the integration of broadband NIRS and EEG to assess neurovascular and neurometabolic coupling. *Sci Rep* 2021; 11: 3977.
11. Kaur J, Fahmy LM, Davoodi-Bojd E, et al. Waste clearance in the brain. *Front Neuroanat* 2021; 15: 665803.
12. Siesjo BK. *Brain energy metabolism*. New York, USA: Wiley and Sons, Ltd., 1978.
13. Boron WF and Boulpaep EL. *Medical physiology: a cellular and molecular approach*. Philadelphia, PA: Saunders, 2003.
14. Deng RM, Liu YC, Li JQ, et al. The role of carbon dioxide in acute brain injury. *Med Gas Res* 2020; 10: 81–84.
15. Chen JJ, Uthayakumar B and Hyder F. Mapping oxidative metabolism in the human brain with calibrated fMRI in health and disease. *J Cereb Blood Flow Metab* 2022; 42: 1139–1162.
16. Yoon S, Zuccarello M and Rapoport RM. pCO(2) and pH regulation of cerebral blood flow. *Front Physiol* 2012; 3: 365.
17. Aram JA and Lodge D. Epileptiform activity induced by alkalosis in rat neocortical slices: block by antagonists of N-methyl-D-aspartate. *Neurosci Lett* 1987; 83: 345–350.
18. Balestrino M and Somjen GG. Concentration of carbon dioxide, interstitial pH and synaptic transmission in hippocampal formation of the rat. *J Physiol* 1988; 396: 247–266.
19. Lee J, Taira T, Pihlaja P, et al. Effects of CO_2 on excitatory transmission apparently caused by changes in intracellular pH in the rat hippocampal slice. *Brain Res* 1996; 706: 210–216.
20. Chesler M. Regulation and modulation of pH in the brain. *Physiol Rev* 2003; 83: 1183–1221.
21. Capps RT. Carbon dioxide. *Clin Anesth* 1968; 3: 122–134.
22. Guaranha MS, Garzon E, Buchpiguel CA, et al. Hyperventilation revisited: physiological effects and efficacy on focal seizure activation in the era of video-EEG monitoring. *Epilepsia* 2005; 46: 69–75.
23. Datto C, Rai AK, Ilivicky HJ, et al. Augmentation of seizure induction in electroconvulsive therapy: a clinical reappraisal. *J Ect* 2002; 18: 118–125.

24. Brian JE Jr. Carbon dioxide and the cerebral circulation. *Anesthesiology* 1998; 88: 1365–1386.
25. Ito H, Kanno I, Ibaraki M, et al. Changes in human cerebral blood flow and cerebral blood volume during hypercapnia and hypocapnia measured by positron emission tomography. *J Cereb Blood Flow Metab* 2003; 23: 665–670.
26. Battisti-Charbonney A, Fisher J and Duffin J. The cerebrovascular response to carbon dioxide in humans. *J Physiol* 2011; 589: 3039–3048.
27. Posse S, Kemna LJ, Elghahwagi B, et al. Effect of graded hypo- and hypercapnia on fMRI contrast in visual cortex: quantification of T(*)(2) changes by multiecho EPI. *Magn Reson Med* 2001; 46: 264–271.
28. Milej D, He L, Abdalmalak A, et al. Quantification of cerebral blood flow in adults by contrast-enhanced near-infrared spectroscopy: Validation against MRI. *J Cereb Blood Flow Metab* 2020; 40: 1672–1684.
29. Chen TW, Wardill TJ, Sun Y, et al. Ultrasensitive fluorescent proteins for imaging neuronal activity. *Nature* 2013; 499: 295–300.
30. Baker KL, Vasan G, Gumaste A, et al. Spatiotemporal dynamics of odor responses in the lateral and dorsal olfactory bulb. *PLoS Biol* 2019; 17: e3000409.
31. Sanganahalli BG, Herman P and Hyder F. Frequency-dependent tactile responses in rat brain measured by functional MRI. *NMR Biomed* 2008; 21: 410–416.
32. Sanganahalli BG, Bailey CJ, Herman P, et al. Tactile and non-tactile sensory paradigms for fMRI and neurophysiologic studies in rodents. *Methods Mol Biol* 2009; 489: 213–242.
33. Fukuda M, Vazquez AL, Zong X, et al. Effects of the alpha(2)-adrenergic receptor agonist dexmedetomidine on neural, vascular and BOLD fMRI responses in the somatosensory cortex. *Eur J Neurosci* 2013; 37: 80–95.
34. Sanganahalli BG, Baker KL, Thompson GJ, et al. Orthonasal versus retronasal glomerular activity in rat olfactory bulb by fMRI. *Neuroimage* 2020; 212: 116664.
35. Sanganahalli BG, Thompson GJ, Parent M, et al. Thalamic activations in rat brain by fMRI during tactile (forepaw, whisker) and non-tactile (visual, olfactory) sensory stimulations. *PLoS One* 2022; 17: e0267916.
36. Nattie EE. Central chemosensitivity, sleep, and wakefulness. *Respir Physiol* 2001; 129: 257–268.
37. Parent M, Li Y, Santhakumar V, et al. Alterations of parenchymal microstructure, neuronal connectivity, and cerebrovascular resistance at adolescence after mild-to-moderate traumatic brain injury in early development. *J Neurotrauma* 2019; 36: 601–608.
38. Parent M, Chitturi J, Santhakumar V, et al. Kaempferol treatment after traumatic brain injury during early development mitigates brain parenchymal microstructure and neural functional connectivity deterioration at adolescence. *J Neurotrauma* 2020; 37: 966–974.
39. Ma Y, Shaik MA, Kozberg MG, et al. Resting-state hemodynamics are spatiotemporally coupled to synchronized and symmetric neural activity in excitatory neurons. *Proc Natl Acad Sci U S A* 2016; 113: E8463–E8471.
40. Wright PW, Brier LM, Bauer AQ, et al. Functional connectivity structure of cortical calcium dynamics in anesthetized and awake mice. *PLoS One* 2017; 12: e0185759.
41. Park K, Liyanage AC, Koretsky AP, et al. Optical imaging of stimulation-evoked cortical activity using GCaMP6f and jRGECO1a. *Quant Imaging Med Surg* 2021; 11: 998–1009.
42. Sanganahalli BG, Rebello MR, Herman P, et al. Comparison of glomerular activity patterns by fMRI and calcium imaging: implications for principles underlying odor mapping. *Neuroimage* 2016; 126: 208–218.
43. Lake EMR, Ge X, Shen X, et al. Simultaneous cortex-wide fluorescence Ca(2+) imaging and whole-brain fMRI. *Nat Methods* 2020; 17: 1262–1271.
44. O'Connor D, Mandino F, Shen X, et al. Functional network properties derived from wide-field calcium imaging differ with wakefulness and across cell type. *Neuroimage* 2022; 264: 119735.
45. Hosford PS, Wells JA, Nizari S, et al. CO(2) signaling mediates neurovascular coupling in the cerebral cortex. *Nat Commun* 2022; 13: 2125.
46. Dulla CG, Dobelis P, Pearson T, et al. Adenosine and ATP link PCO2 to cortical excitability via pH. *Neuron* 2005; 48: 1011–1023.
47. Han Y, Heuermann RJ, Lyman KA, et al. HCN-channel dendritic targeting requires bipartite interaction with TRIP8b and regulates antidepressant-like behavioral effects. *Mol Psychiatry* 2017; 22: 458–465.
48. Dale N. The acid nature of CO2-evoked adenosine release in the CNS. *J Physiol* 2006; 574: 633.
49. Horvath I, Sandor NT, Ruttner Z, et al. Role of nitric oxide in regulating cerebrocortical oxygen consumption and blood flow during hypercapnia. *J Cereb Blood Flow Metab* 1994; 14: 503–509.
50. Li MH, Liu SQ, Inoue K, et al. Acid-sensing ion channels in mouse olfactory bulb M/T neurons. *J Gen Physiol* 2014; 143: 719–731.
51. Krishtal O. The ASICs: signaling molecules? Modulators? *Trends Neurosci* 2003; 26: 477–483.
52. Cristofori-Armstrong B and Rash LD. Acid-sensing ion channel (ASIC) structure and function: Insights from spider, snake and sea anemone venoms. *Neuropharmacology* 2017; 127: 173–184.
53. Kida I, Rothman DL and Hyder F. Dynamics of changes in blood flow, volume, and oxygenation: implications for dynamic functional magnetic resonance imaging calibration. *J Cereb Blood Flow Metab* 2007; 27: 690–696.
54. Herman P, Sanganahalli BG, Blumenfeld H, et al. Quantitative basis for neuroimaging of cortical laminae with calibrated functional MRI. *Proc Natl Acad Sci U S A* 2013; 110: 15115–15120.
55. Paxinos G and Franklin KBJ. *The mouse brain in stereotaxic coordinates*. Compact 2nd ed. Amsterdam; Boston: Elsevier Academic Press, 2004.
56. Englund EK, Fernandez-Seara MA, Rodriguez-Soto AE, et al. Calibrated fMRI for dynamic mapping of CMRO (2) responses using MR-based measurements of whole-brain venous oxygen saturation. *J Cereb Blood Flow Metab* 2020; 40: 1501–1516.

57. Xu F, Uh J, Brier MR, et al. The influence of carbon dioxide on brain activity and metabolism in conscious humans. *J Cereb Blood Flow Metab* 2011; 31: 58–67.
58. Chen JJ and Pike GB. Global cerebral oxidative metabolism during hypercapnia and hypocapnia in humans: implications for BOLD fMRI. *J Cereb Blood Flow Metab* 2010; 30: 1094–1099.
59. Jain V, Langham MC, Floyd TF, et al. Rapid magnetic resonance measurement of global cerebral metabolic rate of oxygen consumption in humans during rest and hypercapnia. *J Cereb Blood Flow Metab* 2011; 31: 1504–1512.
60. Marshall O, Uh J, Lurie D, et al. The influence of mild carbon dioxide on brain functional homotopy using resting-state fMRI. *Hum Brain Mapp* 2015; 36: 3912–3921.
61. Driver ID, Wise RG and Murphy K. Graded hypercapnia-calibrated BOLD: beyond the iso-metabolic hypercapnic assumption. *Front Neurosci* 2017; 11: 276.
62. Hall EL, Driver ID, Croal PL, et al. The effect of hypercapnia on resting and stimulus induced MEG signals. *Neuroimage* 2011; 58: 1034–1043.
63. Kida I, Kennan RP, Rothman DL, et al. High-resolution CMR(O_2) mapping in rat cortex: a multiparametric approach to calibration of BOLD image contrast at 7 tesla. *J Cereb Blood Flow Metab* 2000; 20: 847–860.
64. Shu CY, Herman P, Coman D, et al. Brain region and activity-dependent properties of M for calibrated fMRI. *Neuroimage* 2016; 125: 848–856.
65. Gottler J, Kaczmarz S, Kallmayer M, et al. Flow-metabolism uncoupling in patients with asymptomatic unilateral carotid artery stenosis assessed by multi-modal magnetic resonance imaging. *J Cereb Blood Flow Metab* 2019; 39: 2132–2143.
66. Xu M, Bo B, Pei M, et al. High-resolution relaxometry-based calibrated fMRI in murine brain: metabolic differences between awake and anesthetized states. *J Cereb Blood Flow Metab* 2022; 42: 811–825.
67. Zhang M, Qin Q, Zhang S, et al. Aerobic glycolysis imaging of epileptic foci during the inter-ictal period. *EBioMedicine* 2022; 79: 104004.
68. Sheng M, Liu P, Mao D, et al. The impact of hyperoxia on brain activity: a resting-state and task-evoked electroencephalography (EEG) study. *PLoS One* 2017; 12: e0176610.
69. Hoge RD. Calibrated fMRI. *Neuroimage* 2012; 62: 930–937.
70. Germuska M, Chandler H, Okell T, et al. A frequency-domain machine learning method for dual-calibrated fMRI mapping of oxygen extraction fraction (OEF) and cerebral metabolic rate of oxygen consumption (CMRO(2)). *Front Artif Intell* 2020; 3
71. Berman AJL, Mazerolle EL, MacDonald ME, et al. Gas-free calibrated fMRI with a correction for vessel-size sensitivity. *Neuroimage* 2018; 169: 176–188.
72. Hyder F, Rothman DL and Bennett MR. Cortical energy demands of signaling and nonsignaling components in brain are conserved across mammalian species and activity levels. *Proc Natl Acad Sci U S A* 2013; 110: 3549–3554.
73. Banoub M, Tetzlaff JE and Schubert A. Pharmacologic and physiologic influences affecting sensory evoked potentials: implications for perioperative monitoring. *Anesthesiology* 2003; 99: 716–737.
74. Iida H, Ohata H, Iida M, et al. Isoflurane and sevoflurane induce vasodilation of cerebral vessels via ATP-sensitive K+ channel activation. *Anesthesiology* 1998; 89: 954–960.
75. Driver ID, Whittaker JR, Bright MG, et al. Arterial CO2 fluctuations modulate neuronal rhythmicity: implications for MEG and fMRI studies of Resting-State networks. *J Neurosci* 2016; 36: 8541–8550.
76. Zappe AC, Uludağ K, Oeltermann A, et al. The influence of moderate hypercapnia on neural activity in the anesthetized nonhuman primate. *Cereb Cortex* 2008; 18: 2666–2673.
77. Lohr C, Beiersdorfer A, Fischer T, et al. Using genetically encoded calcium indicators to study astrocyte physiology: a field guide. *Front Cell Neurosci* 2021; 15: 690147.
78. Mishra SK, Herman P, Crair M, et al. Fluorescently-tagged magnetic protein nanoparticles for high-resolution optical and ultra-high field magnetic resonance dual-modal cerebral angiography. *Nanoscale* 2022; 14: 17770–17788.